Journal of Materials Chemistry C

PAPER

View Article Online
View Journal | View Issue

Published on 25 November 2015. Downloaded by Georgia Institute of Technology on 23/12/2016 16:28:28.

Cite this: J. Mater. Chem. C, 2016, 4, 3747

Do charges delocalize over multiple molecules in fullerene derivatives?†

G. D'Avino,[a] Y. Olivier,[a] L. Muccioli*[b] and D. Beljonne*[a]

Received 12th October 2015,
Accepted 23rd November 2015

DOI: 10.1039/c5tc03283k

www.rsc.org/MaterialsC

We address the question of charge delocalization in amorphous and crystalline fullerene solids by performing state of the art calculations encompassing force-field molecular dynamics, microelectrostatic and quantum-chemical methods. The solution of a tight-binding model built from spatially (down to atomistic scale) and time (down to fs) resolved calculations yields the density of electronic states for the charge carriers and their energy-dependent intermolecular delocalization. Both pristine C_{60} and the soluble $PC_{61}BM$/$PC_{71}BM$ acceptors may sustain high-energy states that spread over a few tens of molecules irrespective of morphology, yet electrostatic disorder (mostly dipolar and static in nature) makes the thermally available electron states collapse to hardly more than one molecule in $PC_{61}BM$/$PC_{71}BM$, while it has a much more limited impact in the case of the bare C_{60}. Implications of these results for charge transport and exciton dissociation at donor–fullerene interfaces are discussed.

1. Introduction

Fullerenes are ubiquitous electron acceptor molecules for organic photovoltaics.[1] While C_{60} is typically deposited as thin layers in planar junction architectures using thermal evaporation techniques, the use of its soluble phenyl-C61-butyric acid methyl ester ($PC_{61}BM$) and phenyl-C71-butyric acid methyl ester ($PC_{71}BM$) derivatives, cast from a solution of the donor–acceptor mixture,[2] has paved the way to the bulk heterojunction strategy.[3,4] Despite many attempts to find alternative acceptors,[5–7] fullerenes appear to offer a rather unique combination of attractive (supra)molecular features that turn into solar cells with still the highest power conversion efficiencies. These advantages include of course their relatively high electron affinity compared to common donors, thereby ensuring the necessary driving force for photogeneration, but also the three-dimensional character of the molecular packing that translates into an increased number of pathways for charge transport[8–10] and an entropic gain for exciton dissociation.[11–13] Solution processability and spontaneous nanosegregation into bi-continuous networks when mixed with the molecular or polymer donor represent additional advantages of PCBM.[14,15]

Though some questions are left open, there is growing experimental evidence that, in blends where crystallization of fullerene aggregates occurs in the donor matrix, charge photogeneration at the polymer/fullerene interface proceeds *via* weakly bound charge-transfer excitations.[16–21] Although this is not inconsistent with a localized charge picture,[61,62] it seems that the large coordination shell and high dimensionality of fullerenes, combined with the relatively low intramolecular reorganization energy of the rigid C_{60} cage,[22–25] prompt the formation of electronic states that spread out spatially over neighboring acceptor molecules, thereby reducing the effective Coulomb binding energy of the interfacial electron–hole pairs down to values comparable to k_BT at room temperature.[26] The formation of such delocalized electron wavefunctions is also supported by quantum-chemical calculations and has brought many authors to question the applicability of electron hopping models in these materials.[27,28] Though there is, to our knowledge, no unambiguous proof for a band-like transport mechanism in bulk fullerenes, this would look at first sight consistent with the high electron mobility values (up to 11 $cm^2\ V^{-1}\ s^{-1}$) reported in field effect transistors built from solution-grown aligned C_{60} single crystals.[29,30] In contrast, the electron mobility for the solution-processed fullerene derivatives is typically two or three orders of magnitude smaller,[31] a difference loosely attributed to disorder effects. Theoretical modeling has so far focused primarily on the role played by intermolecular couplings and the large coordination shells of fullerenes that, in conjunction with small intramolecular geometric relaxation energies, are expected to result in sizeable intermolecular delocalization of the electron wavefunction.[22,27,28,32–35] Yet, until recently,[25] computational studies have largely ignored the important fluctuations in

[a] Laboratory for Chemistry of Novel Materials, University of Mons, 7000 Mons, Belgium. E-mail: David.Beljonne@umons.ac.be
[b] Laboratoire de Chimie des Polymères Organiques, UMR 5629, University of Bordeaux, 33607 Pessac, France. E-mail: Luca.Muccioli@u-bordeaux.fr

† Electronic supplementary information (ESI) available: IPR calculated with magnified or reduced electronic couplings; radial distribution functions; validation of ZINDO transfer integral calculations; correlation between electrostatic and induction components of polarization energies; fit of the low energy tails of the density of states; densities of states and IPRs obtained with different approximations of fullerene LUMO degeneracy. See DOI: 10.1039/c5tc03283k

Published on 25 November 2015. Downloaded by Georgia Institute of Technology on 23/12/2016 16:28:28.

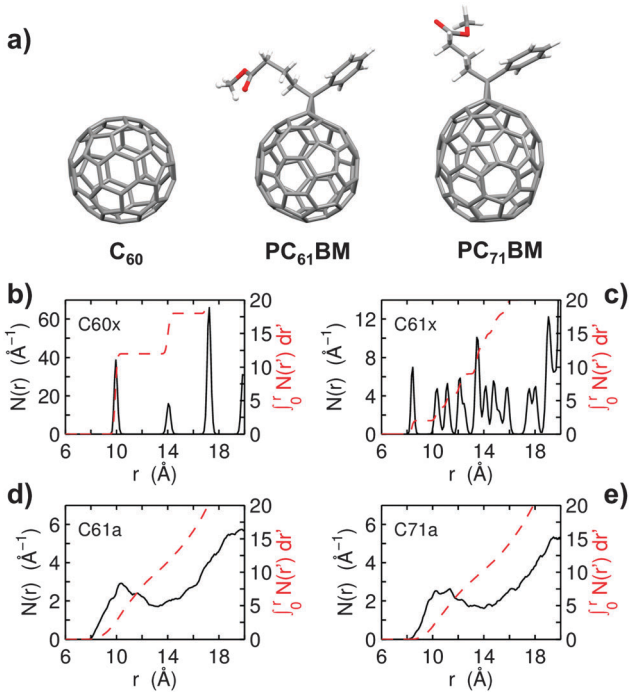

Fig. 1 (a) 3D rendering of the chemical structure of fullerene (C_{60}), phenyl-C_{61}-butyric acid methyl ester ($PC_{61}BM$), and phenyl-C_{71}-butyric acid methyl ester ($PC_{71}BM$). (b–e) Density of neighbours (black continuous lines) and integrated number of neighbours (coordination number CN, red dashed line) as a function of the intermolecular distance, calculated between the centers of mass.

site energies brought about by the polar side groups of PCBM molecules, and whether these could cause or not electron localization.

Hence the question we would like to address in this contribution: how much do excess negative charges delocalize in fullerenes and how does localization depend on the detailed molecular structure (C_{60} *vs.* $PC_{61}BM$ and $PC_{71}BM$, Fig. 1a) as well as on the associated morphology (single crystals *versus* amorphous structures)? To answer these questions, we resort to a full atomistic model that accounts for the thermal fluctuations of the molecular electron energies due to the local dielectric environment and of the intermolecular electronic couplings on an equal footing.

2. Methods

A comprehensive picture of the electronic structure of fullerene derivatives is here obtained by means of a multiscale theoretical approach that synergistically combines different computational methods. This strategy is applied to crystalline C_{60} (labeled "C60x") and $PC_{61}BM$ ("C61x"), and to amorphous phases of $PC_{61}BM$ and $PC_{71}BM$ ("C61a" and "C71a").

Molecular dynamics (MD) simulations are employed to sample the thermal motion and to obtain realistic morphologies for amorphous samples. For each system, MD structures are then used to build a model Hamiltonian for the states relevant to electron transport, developed on the basis of diabatic states localized over molecular units. Model parameters are assessed *via* quantum chemical and microelectrostatic (ME) calculations, accounting for fluctuations of site energies (diagonal disorder) and intermolecular couplings (off-diagonal disorder). The diagonalization of the Hamiltonian provides the adiabatic, and possibly delocalized, states of the molecular solid. Ensemble averages are obtained by repeating this analysis for 11 frames extracted at 2 ns intervals from the MD trajectory.

We present below the calculation details in a top-down fashion, *i.e.* starting from the macroscopic model and then presenting its microscopic ingredients.

2.1. Tight-binding model

The states relevant to electron transport were described by a three-band tight-binding Hamiltonian explicitly accounting for the three low-lying unoccupied orbitals of fullerene derivatives (LUMO, LUMO+1 and LUMO+2), following Troisi and coworkers.[9,27] Our model Hamiltonian reads:

$$H_e = \sum_{m=1}^{N}\sum_{k=1}^{3}\left(\varepsilon_m^k + P_m{}^-\right)|m,k\rangle\langle m,k| + \sum_{m,n}\sum_{k,l=1}^{3} J_{mn}^{kl}\left(|m,k\rangle\langle n,l| + H.c.\right) \quad (1)$$

where m and n run on molecular sites and k and l on the unoccupied orbitals. Diagonal site energies are the sum of two terms, the orbital energies ε_m^k (see Section 2.3), and the electron polarization energy $P_m{}^-$ (see Section 2.4). The polarization energy accounts for the electrostatic interaction of the localized carrier with the relaxed polarizable environment.[36–39] This approach implicitly assumes that molecular induction (sub-fs timescale) is instantaneous with respect to charge transfer (ps timescale).[38] J_{mn}^{kl} are the intermolecular couplings or charge transfer integrals (see Section 2.3), periodic boundary conditions in three directions were implemented to minimize finite-size effects.

Besides Hamiltonian (1), we also considered a simpler model with one orbital per site. There, either the actual LUMO or an "effective" LUMO was used. In the latter case, the site energy is taken as the energy of the LUMO, but we adopted an effective intermolecular coupling $J_{\mathrm{eff}}^{mn} = \sqrt{\sum_{kl}\left(J_{mn}^{kl}\right)^2/3}$ that ensures the same electron-transfer rate of the three explicit orbital picture.

The degree of electron delocalization in the j-th eigenstate is quantified by the inverse participation ratio (IPR):

$$\mathrm{IPR}_j = \left(\sum_{m=1}^{N}\left|p_{mj}\right|^2\right)^{-1} \quad (2)$$

where $p_{mj} = \sum_{k=1}^{3}\left|c_{mj}^k\right|^2$ is the occupation of molecule m in the eigenstate j. We note that our electronic picture, as it disregards polaronic effects, provides an upper estimate of charge delocalization, though the rigidity of fullerene cage suggests a limited influence of molecular relaxation.

This journal is © The Royal Society of Chemistry 2016

Published on 25 November 2015. Downloaded by Georgia Institute of Technology on 23/12/2016 16:28:28.

The density of carriers, given as the fraction of charged molecules ($n = N_{el}/N_{mol}$), relates to the density of states (DOS) and to the Fermi energy (E_F) *via* the equation:[40]

$$n(E_F) = \int \mathrm{DOS}(E) \frac{1}{1+\exp[(E-E_F)/(kT)]} \mathrm{d}E \qquad (3)$$

This integral is evaluated using an analytical expression to fit the low-energy tail of the DOS obtained from numerical calculations. Details on the fit can be found in the ESI.† We inverted the $n(E_F)$ curve in order to obtain the Fermi energy for a sensible range of carrier concentration.[41]

2.2. Molecular dynamics simulations

The crystalline samples were built as replica of the experimental crystal unit cells. Crystalline supercells (counting 500 and 576 molecules in C60x and C61x, respectively) were equilibrated at atmospheric pressure and room temperature (300 K), utilizing a weak coupling barostat, a velocity-scaling thermostat, and smooth particle mesh Ewald method for electrostatic interaction. The crystal structure of fullerene is known since the discovery of this material in 1985, and we used here a well resolved one available in the literature,[42] while for $PC_{61}BM$ a solvent-free structure has been reported only very recently;[43,44] the crystal structure of $PC_{71}BM$ is so far unknown. Amorphous samples of 512 molecules each were instead produced starting from very low-density configurations that were first annealed for a few ns at 2000 K and at constant volume. These were then compressed and equilibrated at the same conditions employed for crystalline samples.

For the force field, the choice went to a united atom force field (with implicit hydrogens) that was already employed for simulating crystalline fullerene[45] and $PC_{61}BM$.[26] In C_{60}, all atoms are charge-less, while for $PC_{61}BM$ and $PC_{71}BM$ we adopted an identical set of charges at heavy atoms, obtained by electrostatic potential fitting from B3LYP/cc-pVTZ calculations. Charges were symmetrized and slightly adapted in order to have only the half of the fullerene cage closer to the phenyl-butyric acid substituents with non-zero charges. All simulations were carried out with NAMD 2.8,[46] with an equilibration time of at least 30 ns and production time of 20 ns.

2.3. Semiempirical quantum-chemical calculations

Orbital energies ε_m^k and transfer integrals J_{mn}^{kl} were both computed at the (Z)INDO level. Once validated *versus* higher level calculations, semiempirical methods represent an affordable and reliable option to perform many thousands of calculations for several MD frames.

The energies ε_m^k of the unoccupied orbitals LUMO+k, with k = 0, 1, 2, were calculated for isolated molecules at the MD geometry. When introducing ε_m^k in Hamiltonian (1), an energy shift was applied so that the LUMO energy amounts to −2.7 eV. Experiments and high-level calculations in fact indicate electron affinity (EA) to pin at about 2.7 ± 0.1 eV for C_{60}, $PC_{61}BM$ and $PC_{71}BM$.[47–50] Hence, we used ZINDO only to capture the relative energy difference between LUMO levels and their variation with the molecular geometry in the solid state.

The electron transfer integrals J_{mn}^{kl} were calculated in the one-electron picture between the kth and lth orbitals of molecules m and n, respectively.[51] In fact, considering three LUMOs implies that all nine electronic couplings between the LUMO+k and LUMO+l (with k and l going from 0 to 2) are accounted for in the evaluation of the DOS, ODOS, and IPR. In general, charge transfer integral is a delicate quantity to compute: it has been shown to depend crucially on the method (DFT, Hartree–Fock),[52,53] the functional,[52] the basis set,[54] as well as the diabatization scheme (Constrained DFT, Fragment Orbital DFT).[53] As a validation step prior to larger scale calculations on the MD morphologies, we compared ZINDO transfer integrals with the results of recent calculations by Blumberger and coworkers at the fragment orbital density functional theory (FODFT) level.[22,53] As reported in Fig. S2 (ESI†), we found a reasonably good agreement between the effective intermolecular coupling calculated at the ZINDO level and the scaled FODFT transfer integrals for three different relative orientations of the C_{60} molecules, as well as a function of the relative distance between them. Moreover, as displayed in Table S1 (ESI†), the predicted IPRs are affected by the overall magnitude of the transfer integrals (scaled uniformly with three different scaling factors) in a way that does not alter the general conclusions of this work. Transfer integrals are computed for all the molecular pairs with closest intermolecular atom–atom contact within 8 Å, calculated applying 3D periodic boundary conditions.

2.4. Microelectrostatic calculations

The interaction between charge carriers and the molecular environment is responsible for large variations of site polarization energies of electrons, P_m^-, which we assume to depend only on the molecular site and not on the orbital actually occupied by the extra charge. This quantity is here evaluated with the classical ME model described in ref. 55, based on permanent atomic charges and distributed polarizabilities that give rise to induced dipoles at heavy atoms. Self-consistent ME calculations were performed in order to account for the mutual interactions between induced dipoles.

The set of atomic charges used in ME calculations is identical to the one employed in the MD simulations. Isotropic molecular polarizabilities for neutral and negatively charged fullerenes were calculated with B3LYP//6-311++G** model chemistry (α_{C60} = 81.6 Å^3, α_{C60}^- = 91.3 Å^3, α_{PC61BM} = 106.5 Å^3, α_{PC61BM}^- = 113.2 Å^3, α_{PC71BM} = 126.2 Å^3, α_{PC71BM}^- = 133.1 Å^3). DFT calculations for the parameterization of the ME model were performed with Gaussian 09 A01.[56]

Polarization energies include an electrostatic (S_m^-) and induction term (D_m^-). S_m^- corresponds to the interaction energy required to place the charged molecule in the electrostatic field of the surrounding non-polarized molecules, while $D_m^- < 0$ is the stabilizing contribution provided by the dipoles induced by the localized charge. The induction term D_m^- is obtained in the bulk limit by extrapolating the results of self-consistent calculations on spherical clusters with radius of R = 30, 35, 40, and 45 Å (consisting of approximately N = 100–600 molecules) by the linear fit $D(R^{-1}) = D_m^- + c \cdot R^{-1}$.

Published on 25 November 2015. Downloaded by Georgia Institute of Technology on 23/12/2016 16:28:28.

The electrostatic term S_m^- is instead evaluated for the largest cluster, and the total polarization energy for molecule m is just $P_m^- = S_m^- + D_m^-$. Polarization energies obtained in this way target the value for a 3D bulk solid. The calculation of polarization energies for all the molecules in our samples represented the most computationally demanding step of our modeling.

3. Results and discussion

3.1. Structural characterization and connectivity

We begin our analysis with the discussion of the molecular dynamics simulation results. This is an important step, not only as the structure affects all the electronic properties of a given material, but also because the comparison with experimental data is often straightforward and may serve for evaluating the quality of the force field and how far the simulated system is from reality.[57] Here in particular we can compare, at least for C60x and C61x, the simulated and experimental densities and cell parameters, alongside with MD results in the literature[44] (Table 1). All the experimental values are nicely reproduced for C60x, while for C61x the cell parameter b is slightly underestimated, yet the calculated density is still in good agreement with the experimental one (1.65 g cm^{-3} *vs.* 1.62 in single crystals[43] and 1.69 g cm^{-3} in thin films[58]). Amorphous samples C61a and C71a show very similar densities (1.55–1.56 g cm^{-3}) and remarkably lower than the one of C61x. The C71a density is very close to the one obtained at room temperature with MD simulations by Williams and co. (1.57 g cm^{-3}); on the contrary they found slightly lower densities for C61a (1.51 g cm^{-3}).[59]

A first insight into the molecular organization is given by the radial density of neighboring molecules $N(r)$, shown with black continuous lines in Fig. 1b–e for our four samples. The $N(r)$ of C60x and C61x presents a series of well resolved peaks typical of crystalline samples and the large difference between the two originates from the different cell symmetry: for the face-centered cubic C60x there is only one type of first neighbors at $r \approx 10$ Å, while for the monoclinic C61x the situation is more complex with several peaks appearing in sequence. The trend of $N(r)$ confirms the similarity of C61a and C71a. Both amorphous samples in fact show only a broad peak for the first coordination shell at about 10 Å, then a region still populated but not as dense at the first one, and then a continuous rise typical of an isotropic distribution of molecules with $N(r) \propto r^2$.

The number of neighbors around one molecule (the coordination number, CN) is better summarized by the cumulative integral of $N(r)$, shown again in Fig. 1b–e with dashed red lines. For the crystalline samples it grows in steps centered at the positions of the main $N(r)$ peaks; the 12 neighbours of C60x cubic-centered lattice are recovered at $r \approx 10$ Å (18 at $r \approx 14$ Å), while for C61x the coordination number is less well defined, appeareing to be CN = 7 when the distance between fullerene groups is considered,[43,44] or CN = 9 at $r \approx 13$ Å, using the distance between the centers of mass in the calculation. For the amorphous C61a and C71a samples the number of neighbors instead rises in a rather continuous fashion, starting from CN = 1 at $r \approx 9$ Å, and reaching CN = 10 at about $r \approx 13$ Å; the main difference between the two is that the curves for C71a is shifted by $\approx$0.5 Å to larger r, owing to the larger molecular size of the C_{70} cage.[59] In general, even though here larger samples and longer simulation times are spanned with a united atom force field, the morphological picture that is obtained is very similar to recent fully atomistic MD studies (ref. 44 for C61x, ref. 32 for C61a, ref. 59 for C71a).

Once having assessed the local structure around the molecules, it is worth investigating how much this is relevant for the effective electronic connectivity between them. We hence analyze the electronic couplings for electron transfer, which, directly mirroring wavefunction overlap, are highly sensitive to the distance and relative orientation between the molecules, as well as to thermal lattice fluctuations sampled along MD simulations.[60]

The ensemble-averaged value of the effective coupling J_{eff} with the inter-fullerene distance is shown in Fig. 2a. The decay with distance is roughly exponential, as often assumed in lattice models for charge transport, but with long-range tails and large standard deviations at any distance. In addition, the larger and anisotropic C_{70} unit determines a longer decay length in C71x, while the curves for C_{60} derivatives are very similar among them. This information is integrated by the energy distribution of LUMO–LUMO transfer integrals in Fig. 2b. For all the systems we found that couplings between individual orbitals are in the 0–30 meV range, in line with similar calculations by Brédas and coworkers,[59] with nearly identical distributions for transfer integrals between other unoccupied orbitals (not shown). Electronic couplings are, however, on average much stronger in the highly symmetric and densely packed C60x, hinting to a qualitatively different nature of charge transport for this system. On the other hand, the distributions for PCBMs are rather similar, especially in the region of larger couplings.

Finally, Fig. 2c shows the electronic connectivity or effective coordination number, defined as the number of neighbors having, on average, J_{eff} larger than a given value. This plot shows that the actual coordination does not necessarily follow the one guessed from the structure (see Fig. 1b–e). In fact, while for C60x we have 12 neighbors with sizeable couplings ($J_{\text{eff}} > 5$ meV) as expected, values between 6 and 7 are found for the PCBMs. Quite surprisingly, we note that the electronic connectivity is higher in

Table 1 Experimental and simulated densities and cell parameters for C_{60}, $PC_{61}BM$, and $PC_{71}BM$

System	Density (g cm^{-3})	a (Å)	b (Å)	c (Å)	α (deg)	β (deg)	γ (deg)
C60x exp.[a]	1.73	14.05	14.05	14.05	90	90	90
C60x MD[b]	1.72	14.1	14.1	14.1	90[h]	90[h]	90[h]
C61x exp.[c]	1.63	13.47	15.14	19.01	90	106.9	90
C61x exp.[d]	1.62	13.50	15.16	19.10	90[h]	107.1	90[h]
C61x MD[e]	1.63	13.3	14.9	19.5	90[h]	106.3	90[h]
C61x MD[f]	1.65	13.5	14.8	19.2	90[h]	106.8	90[h]
C61a MD[g]	1.56	—	—	—	—	—	—
C71a MD[g]	1.55	—	—	—	—	—	—

[a] 100 K, 4 molecules per cell, ref. 42. [b] This work, 300 K, 5 × 5 × 5 supercell, 500 molecules. [c] 100 K, 4 molecules per cell, ref. 43. [d] 298 K, 4 molecules per cell, ref. 44. [e] 300 K, 3 × 3 × 3 supercell, 108 molecules, ref. 43. [f] This work, 300 K, 6 × 6 × 4 supercell, 576 molecules. [g] This work, 300 K, 512 molecules. [h] Fixed.

 This journal is © The Royal Society of Chemistry 2016

Published on 25 November 2015. Downloaded by Georgia Institute of Technology on 23/12/2016 16:28:28.

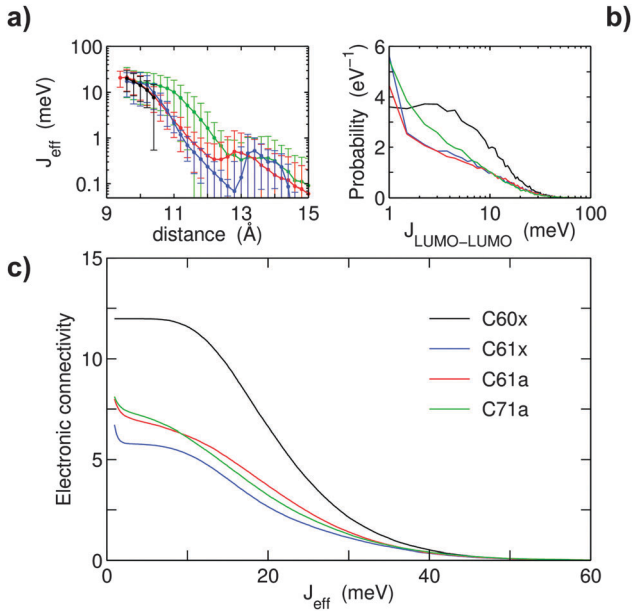

Fig. 2 (a) Average value of the effective transfer integral as a function of the distance between the fullerene cage centers. Error bars represent the standard deviations. (b) Distribution of the LUMO–LUMO transfer integral values in the four systems. (c) Intermolecular electronic connectivity based on effective transfer integrals, defined as the average number of neighbors having a coupling larger than a given J^{eff} value.

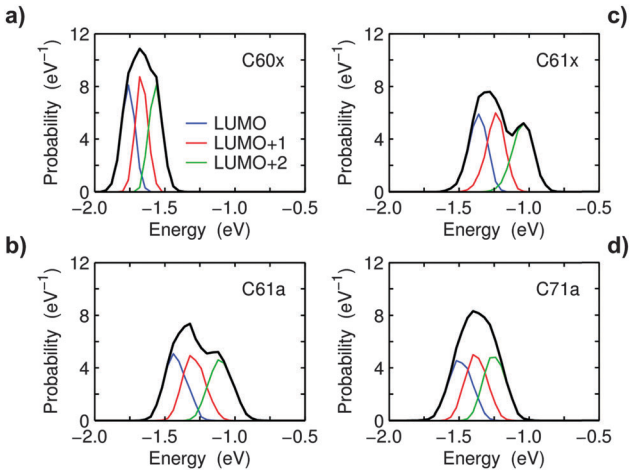

Fig. 3 Distribution of the ZINDO orbital energies calculated for isolated molecules at the simulated morphologies. An energy shift is then applied to these values in building Hamiltonian (1), so that the mean energy of the LUMO is −2.7 eV for all the systems.

amorphous samples than in C61x, suggesting that, unlike other small molecules or polymers, the connectivity between nearly spherical molecules does not suffer from structural disorder.

3.2. Diagonal energetic disorder and polarization energies

We now turn to the analysis of the energy of molecularly confined charge carriers in the different fullerene morphologies, corresponding to the diagonal elements of Hamiltonian (1) and being the sum of the orbital energy and of the polarization energy.

We start the discussion from the LUMO energies, whose distributions for the four systems under examination are shown in Fig. 3. The C_{60} molecule presents a threefold degenerate LUMO when it retains the highest possible symmetry (I_h point group). However, molecular vibrations at room temperature distort molecular geometry leading to a splitting of the three levels that remain close in energy, with a difference of $\approx$0.1 eV between the maxima of their distributions (see Fig. 2a). In substituted fullerenes as $PC_{61}BM$ and $PC_{71}BM$ this degeneracy is lifted but the three LUMOs still remain quite close in energy (within $\approx$0.5 eV, see Fig. 2b–d), while the larger flexibility conferred by the butyric acid methyl ester group results in broader distributions for the individual levels than in C_{60}. The broader LUMOs distributions found for C61a (and C71a) with respect to C61x testify a larger molecular distortion in the amorphous phases.

More interesting is the analysis of polarization energies P^-, quantifying the contribution of the interaction between the localized charge carriers and the neighboring polarized molecules. These environmental effects represent the main source of diagonal disorder in ordered and disordered materials. Within the ME approach, P^- can be cast into an electrostatic (S^-) and an induction (D^-) component (see Section 2.4), as largely documented in previous works.[39,40] Since both contributions are sensitive to the local environment around the charged molecule, P^- changes from site to site and with time.

The ensemble distributions of polarization energies, including electrostatic and induction components, are shown in Fig. 4, while the relevant statistics are reported in Table 2. Polarization energies vary around a mean value of 0.9–1.0 eV for all the investigated systems, and appear to be dominated by the induced dipole contribution, with the electrostatic component very close to zero, on average. However, the electrostatic contribution is the main responsible for the energetic disorder, *i.e.* the standard deviation of the polarization energies.

We notice that accounting for induced dipoles in the calculation, as we do with the ME approach, actually reduces the total disorder with respect to a solely electrostatic picture, as can be seen by comparing the standard deviations of P and S in Table 2. In other words, performing a purely electrostatic calculation based on partial atomic charges (*i.e.* neglecting the role of molecular polarizability) leads to an overestimation of the energetic disorder.[63,64] This result follows from a rather strongly anti-correlation (see ESI† for correlation plots) between S and D that we encountered in the electrostatic modeling of other systems and that we believe to be a general feature of organic materials.

Striking differences appear when comparing the different fullerenes, especially for what concerns the magnitude of the site energy disorder. The disorder mostly originates from the rather large permanent electric dipole in $PC_{61}BM$ and $PC_{71}BM$ (respectively 4.1 and 4.6 Debye at B3LYP/6-31G/6-311++G** level) conferred by the polar butyric acid methyl ester group. In fact C_{60}, which has no permanent dipole, exhibits a very limited disorder in the crystal phase, only 5 meV.

It is also interesting to note that the similarities in the supramolecular structure and in molecular dipole between

Published on 25 November 2015. Downloaded by Georgia Institute of Technology on 23/12/2016 16:28:28.

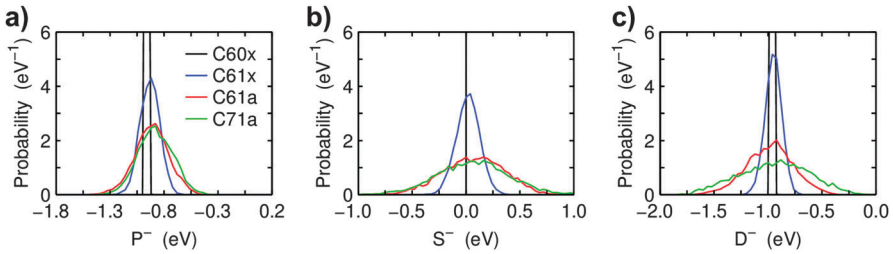

Fig. 4 Distribution of the calculated polarization energies. From the left to the right, (a) total, (b) electrostatic, and (c) induction components. For C60x the S^- distribution is a Dirac delta function centered at zero, and the P^- distribution reaches the value of 25 eV^{-1}.

Table 2 Average polarization energies (total *P*, electrostatic *S*, and induction *D*) and corresponding standard deviations for the four systems studied (units: eV). The "static" or positional standard deviation is also given, evaluated as $\left[\sum(\langle E\rangle - \langle E_i\rangle)^2 / N\right]^{1/2}$ where $\langle E_i\rangle$ is the average energy for molecule *i* along the trajectory, $\langle E\rangle$ is the global average, and *N* is the total number of molecules

System	$\langle P\rangle$	Std *P*	Std P_{pos}	$\langle S\rangle$	Std *S*	Std S_{pos}	$\langle D\rangle$	Std *D*	Std D_{pos}	Std LUMO
C60x	−0.957	0.005	0.001	—	—	—	−0.957	0.005	0.001	0.049
C61x	−0.945	0.085	0.053	0.014	0.109	0.074	−0.959	0.070	0.044	0.068
C61a	−0.915	0.157	0.138	0.069	0.278	0.260	−0.984	0.217	0.206	0.077
C71a	−0.880	0.160	0.143	0.066	0.329	0.314	−0.946	0.321	0.312	0.083

C61a and C71a determine also very similar energetic landscapes. Moreover, the larger positional disorder of amorphous samples translates into a larger inhomogeneous broadening of polarization energies, with the standard deviation that is roughly doubled from the 85 meV of cC61x to the 160 meV in C6(7)1a. The calculated energetic disorder computed for the crystalline C61x sample (100 meV, including the spread of the LUMO energy) compares favorably with the value of 73–77 meV extracted from fitting the temperature-dependent zero field mobility of $PC_{61}BM$,[34,65] though this comparison should be considered with care (as, among others, the fitted value depends on the model used[66]).

Another relevant question is whether the large site energy disorder of fullerene derivatives is static or dynamic. Here, it is useful to consider which kinds of molecular motions characterize the dynamics of these solids. Apart the ubiquitous molecular or lattice vibrations, which take place in the sub-picosecond time scale, PCBM derivatives do rotate at room temperature, like C_{60}, but on a much slower time scale, of the order of hundreds of nanoseconds *versus* the picoseconds for C_{60}.[26,42,45] We measured the timescale of these rotations in our simulations by fitting the time autocorrelation function of the molecular axes (Fig. 5a) with a tri-exponential function, obtaining a rough estimate of 0.05[45] and 1500 ns for C60x and C61x, and of 500 and 600 ns for the amorphous C61a and C71a samples (for the dipole autocorrelation functions in Fig. 5b, C61x: 300 ns, C61a and C71a: 150 ns). This difference should have profound effect on charge transport as in the case of C_{60} small changes in the energy landscape occur while the charge moves, while for the dipolar derivatives the energetic disorder can be considered as static in nature on the time scale of charge transport.

The analysis of rotational motion gives only partial information, since the time autocorrelation function of PCBM molecular dipoles in Fig. 5b shows actually two different decays: a very fast one on the picosecond time scale, which we attribute to molecular and lattice

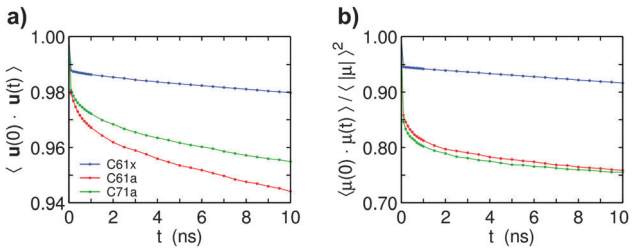

Fig. 5 (a) Time autocorrelation function of an arbitrary molecular axis for $PC_{61}BM$ and $PC_{71}BM$ samples. The corresponding function for C60x is not shown, as the rotation time for at room temperature is of the order of 1 ps.[45] (b) Time autocorrelation function of the molecular dipole unit vector.

vibrations, and a more important and much slower one that corresponds to the molecular rotation. Considering that in the 20 ns time scale spanned by our simulations the molecular rotation of PCBMs is practically negligible, we can disentangle the fraction of the energetic disorder that depends on the position of the molecule in the sample from other contributions evolving on a much faster timescale. We quantified the positional disorder by calculating the standard deviation of the mean polarization energy for each molecule *i* with respect to the global average, $\left[\sum(\langle P\rangle - \langle P_i\rangle)^2 / N\right]^{1/2}$, whose values are reported in Table 2. This analysis shows that the positional electrostatic disorder largely dominates the energetic disorder in amorphous samples and contributes for about 60% to the total disorder in C61x. We also note that the residual (*i.e.* non positional) disorder is similar for amorphous and crystalline PCBMs, hinting to a possible common origin, as for instance the conformational dynamics of the polar side groups. The primarily static nature of the energetic disorder in PCBMs is in line with a very recent study by Tummala *et al.*,[25] though owing to different cluster sizes and methodologies employed in the calculation of site energies,

 This journal is © The Royal Society of Chemistry 2016

Published on 25 November 2015. Downloaded by Georgia Institute of Technology on 23/12/2016 16:28:28.

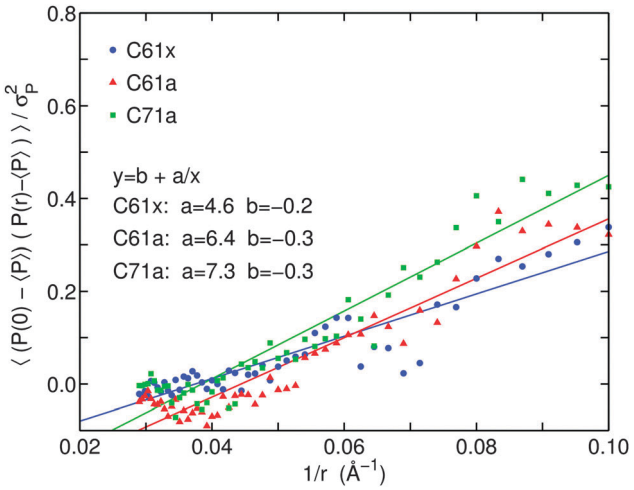

Fig. 6 Spatial correlation function of the static and dynamic polarization energies. Continuous lines correspond to a fit from r = 8 Å onwards of the normalized spatial correlation function of the total polarization energy with an inverse distance dependence equation, following Novikov *et al.*[67,68]

there is only qualitative agreement between the standard deviations reported in Table 2 and their results.

A last word regarding the site energetic disorder concerns the possibility that, being mostly dipolar in nature, the disorder might be spatially correlated. To check this hypothesis, which might have important consequences for charge transport pathways, we computed the spatial correlation function for the polarization energy, Fig. 6. Fitting the data with an inverse distance dependence relation as proposed by Novikov *et al.*,[67,68] we conclude that there is some degree of spatial correlation, yet limited to 2–3 nm, *i.e.* up to the nearest or next-nearest neighbors, with a larger correlation range for $PC_{71}BM$ than for $PC_{61}BM$, an effect directly related to the larger size of the former molecule.

3.3. Density of states and charge delocalization

After having discussed the microscopic electronic parameters and their relationship with the molecular and supramolecular structure, we are in the position of describing the electronic states in the four systems under investigation. The panels in the upper line of Fig. 7 show the density of states (DOS) for localized and possibly delocalized states, *i.e.* the diagonal elements and the eigenstates of Hamiltonian (1), respectively. The density of localized states is approximately Gaussian for all the systems. The partly resolved peaks relative to the different orbitals in Fig. 3b and c are smeared out by the disorder in polarization energies and can be only grasped in the asymmetry of the DOS of C61x. Delocalization effects minimally affect the DOS of PCBMs that essentially remain Gaussian with slightly longer tails, while a considerable change occurs for C_{60} that presents a much steeper decay at its edges.

From the calculated DOS we can extract the electron affinities (EA), accounting for the effect of polarization and charge delocalization on equal footings. For such a purpose, the low-energy tails of the DOSs were fitted with analytic functions and the EA estimated as the x-axis intercept of the tangent to the curve in its steepest point (see ESI† for details and fit parameters). Similar values are obtained for the four systems (EA ≈ 3.8–3.9 eV, see annotations in Fig. 7), in good agreement with the low energy inverse photoemission spectroscopy (LEIPS) data by Yoshida and coworkers, who reported EA values in the 3.7–4.0 eV range for several fullerene derivatives.[69,70] Moreover, our results are also consistent with the 0.12 eV decrease of the EA in $PC_{61}BM$ upon crystallization, recently reported by Zhong *et al.*,[58] and we ascribe this difference to the longer tail in the DOS of the more energetically disordered amorphous system.

The energy distributions of occupied states (or occupied DOS, ODOS) have been computed for a broad range of carrier concentration and are shown in the bottom line panels of Fig. 7. The ODOS, whose shape essentially depends on the tail of the DOS, is much broader in PCBMs than in C_{60}, and especially in the more disordered amorphous systems. The values obtained for the Fermi energy, marked by solid vertical lines in Fig. 7, are in line with experimental data,[49] and can be experimentally tuned by few tenths of eV in disordered systems

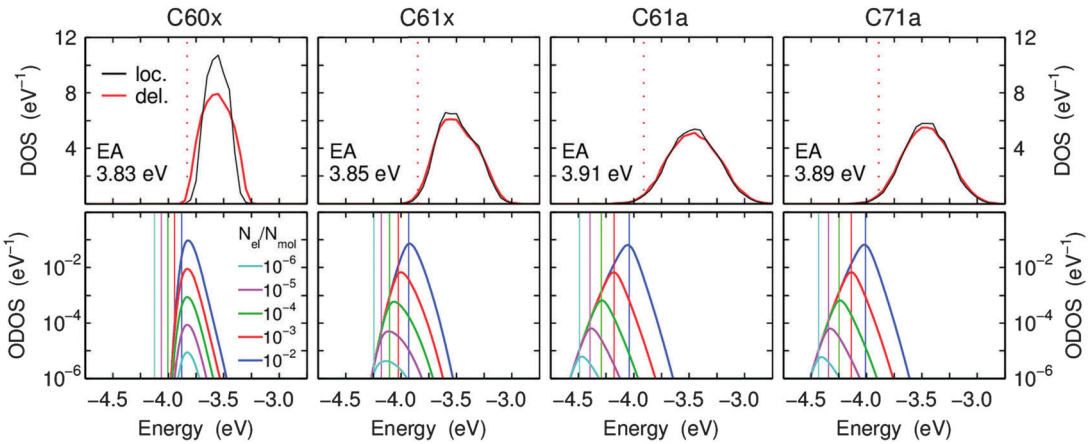

Fig. 7 Top panels: Density of states for the four systems under examination computed for localized and delocalized carriers. The vertical dotted line marks the value of the electron affinity that is also annotated in each graph. Bottom panels: Distributions of occupied states at different carrier densities. Vertical thin lines mark the value of the Fermi energy computed for each density.

Published on 25 November 2015. Downloaded by Georgia Institute of Technology on 23/12/2016 16:28:28.

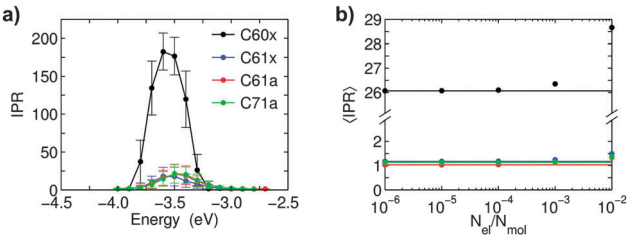

Fig. 8 (a) Distribution of the inverse participation ratio (IPR, eqn (2)) quantifying the number of molecules over which eigenstates are delocalized, as a function of the eigenstate energy. Dots and error bars mark the average and standard deviation of IPR value in intervals of energy. (b) Thermal averages of the IPR at 300 K as a function of the charge carrier density (dots) computed with the Fermi–Dirac statistics. Straight lines are the density-independent Boltzmann thermal averages.

by varying the carrier concentration *via* doping or by applying a gate bias in a field-effect transistor architecture.

We finally address the issue of a possible charge delocalization in fullerene derivatives by inspecting the inverse participation ratio (IPR in eqn (2)) that essentially counts the number of molecules over which electronic states are delocalized. The distributions of IPR values as a function of their eigenstates energies are shown in Fig. 8a. As it is well known for disordered molecular systems, charge delocalization is higher in the central and denser region of the DOS for all the investigated systems, while localized states are found at the edges. Once again, however, C_{60} singles out, with maximum IPR values reaching up to 200 molecules, compared to less than 30 molecules in the soluble fullerene derivatives, irrespective of their morphology. The states at the center of the DOS might have a relevance for charge separation in organic solar cells, provided these higher-lying delocalized acceptor states resonate with molecular donor excitations.[18,71]

To assess the role of delocalization on charge transport, we are instead interested in the thermal averages of the IPR, shown in Fig. 8b as a function of the different carrier concentration using the Fermi–Dirac statistics. A first observation is that thermally-averaged IPR at room temperature barely deviates from the density-independent Boltzmann average (horizontal lines) in the relevant range of carriers concentration. More importantly, we find that states relevant to charge transport are delocalized over $\approx$26 molecules in C_{60}. Though this is an upper estimate based on a purely electronic picture, it is thus likely that a hopping model will fail in qualitatively describing the charge transport properties in unsubstituted C_{60} crystalline samples.

The picture obtained for $PC_{61}BM$ and $PC_{71}BM$ is profoundly different: despite the favorable electronic coordination, the presence of (mostly dipolar-like) static energetic disorder confines the low-energy eigenstates over hardly more than one molecule. Thus, up to high charge carrier densities, our calculations suggest that the wavefunction for the excess electron in PCBM fullerene derivatives is to a good approximation confined over a single molecule. This finding is only in apparent contrast with the theoretical results of Cheung and Troisi,[27] who reported a delocalization over up to 50 molecules for C61a by using a very similar methodology, because they actually neglected the fluctuations of site energies $\varepsilon_m^k + P_m^-$, and consequently obtained an upper limit to charge delocalization. It is also interesting to note that, despite the halved energetic disorder, the thermally averaged IPR for C61x is only slightly larger than that of C61a and C71a.

Before concluding, we note that the amount of charge delocalization is largely underestimated in a minimal model where only the LUMO of each fullerene is considered, although the use of effective electronic couplings (J_{eff}) provides an adequate description of the DOS tail (see ESI† for further details). The latter approach should be adequate for charge transport simulations. Nevertheless, models with one orbital per site cannot describe the DOS as a whole, and in particular higher lying states that have been proposed as one of the key elements for the success of fullerene derivatives as electron acceptor materials in organic solar cells.[9]

4. Conclusions

The modeling studies presented here provide a robust microscopic picture for charged excitations in solid-state fullerenes. By accounting for molecular motion at different timescales and treating intermolecular charge transfer and electrostatic interactions in a polarizable environment on equal footings, we quantified the amount of electron wavefunction delocalization in unsubstituted and substituted fullerenes. Performing these calculations on large samples for multiple snapshots extracted along MD runs yield ensemble distributions and relevant timescales for the fluctuations. In line with earlier theoretical models, our results point to the formation of electronic states that largely spread over at least a few molecular shells, depending on the actual chemical structure and morphology. We conjecture that these states, if hybridized with or thermally accessible from the donor electronic excitations might play a critical role in charge separation at fullerene-based heterojunctions. We are currently conducting similar simulations on polymer–fullerene interfaces to assess how much this true.

It is important to stress, however, that while these spatially delocalized states can be thermally populated in pristine C_{60}, they are found far above the Fermi energy in the soluble $PC_{61}BM$ and $PC_{71}BM$ derivatives. In the latter two materials, irrespective of the actual morphology (crystalline or amorphous), the low-energy tail of the density of states comprises electronic states that hardly extend over more than a single molecule. We calculated the amount of dipolar electrostatic disorder in the fullerene derivatives and identified it as being the main responsible for the collapse of the electronic wavefunction. Besides, such a disorder was found to be primarily static in nature, in comparison to timescales for charge transport, and weakly spatially correlated. Altogether, these results suggest that C_{60} and PCBMs might behave differently in terms of charge transport, with the former closer to a band regime and the latter likely appropriately accounted for in a hopping picture. However, a definitive (dis)proof for this hypothesis calls for charge transport simulations going beyond these two limited scenarios.

 This journal is © The Royal Society of Chemistry 2016

Published on 25 November 2015. Downloaded by Georgia Institute of Technology on 23/12/2016 16:28:28.

Acknowledgements

The work in Bordeaux has been funded by French National Grant ANR-10-LABX-0042-AMADEus managed by the National Research Agency under the initiative of excellence IdEx Bordeaux programme (reference ANR-10-IDEX-0003-02). The work in Mons was supported by the Programme d'Excellence de la Reǵion Wallonne (OPTI2MAT Project) and FNRS-FRFC. D. B. is research director of FNRS. GD acknowledges support from EU through the FP7-PEOPLE-2013-IEF program.

Notes and references

1 S. Kirner, M. Sekita and D. M. Guldi, *Adv. Mater.*, 2014, **26**, 1482–1493.
2 R. Augulis, A. Devižis, D. Peckus, V. Gulbinas, D. Hertel and K. Meerholz, *J. Phys. Chem. C*, 2015, **119**, 5761–5770.
3 A. Diaz de Zerio Mendaza, J. Bergqvist, O. Bäcke, C. Lindqvist, R. Kroon, F. Gao, M. R. Andersson, E. Olsson, O. Inganäs and C. Müller, *J. Mater. Chem. A*, 2014, **2**, 14354.
4 S.-J. Ko, W. Lee, H. Choi, B. Walker, S. Yum, S. Kim, T. J. Shin, H. Y. Woo and J. Y. Kim, *Adv. Energy Mater.*, 2015, **5**, DOI: 10.1002/aenm.201401687.
5 Y. Lin and X. Zhan, *Mater. Horiz.*, 2014, **1**, 470.
6 H. Li, T. Earmme, G. Ren, A. Saeki, S. Yoshikawa, N. M. Murari, S. Subramaniyan, M. J. Crane, S. Seki and S. A. Jenekhe, *J. Am. Chem. Soc.*, 2014, **136**, 14589–14597.
7 G. Sauvé and R. Fernando, *J. Phys. Chem. Lett.*, 2015, **6**, 3770–3780.
8 P. J. Skabara, J.-B. Arlin and Y. H. Geerts, *Adv. Mater.*, 2013, **25**, 1948–1954.
9 T. Liu and A. Troisi, *Adv. Mater.*, 2013, **25**, 1038–1041.
10 N. E. Jackson, B. M. Savoie, L. X. Chen and M. a. Ratner, *J. Phys. Chem. Lett.*, 2015, **1021**, 1018–1021.
11 B. A. Gregg, *J. Phys. Chem. Lett.*, 2011, **2**, 3013–3015.
12 N. R. Monahan, K. W. Williams, B. Kumar, C. Nuckolls and X.-Y. Zhu, *Phys. Rev. Lett.*, 2015, **114**, 247003.
13 T. M. Clarke and J. R. Durrant, *Chem. Rev.*, 2010, **110**, 6736–6767.
14 M. T. Dang, L. Hirsch and G. Wantz, *Adv. Mater.*, 2011, **23**, 3597–3602.
15 J. Maibach, T. Adermann, T. Glaser, R. Eckstein, E. Mankel, A. Pucci, K. Müllen, U. Lemmer, M. Hamburger, T. Mayer and W. Jaegermann, *J. Mater. Chem. C*, 2014, **2**, 7934.
16 G. Grancini, D. Polli, D. Fazzi, J. Cabanillas-Gonzalez, G. Cerullo and G. Lanzani, *J. Phys. Chem. Lett.*, 2011, **2**, 1099–1105.
17 W. L. Leong, G. Hernandez-Sosa, S. R. Cowan, D. Moses and A. J. Heeger, *Adv. Mater.*, 2012, **24**, 2273–2277.
18 H. Ma and A. Troisi, *Adv. Mater.*, 2014, **26**, 6163–6167.
19 S. L. Smith and A. W. Chin, *Phys. Rev. B: Condens. Matter Mater. Phys.*, 2015, **91**, 1–5.
20 S. Gélinas, A. Rao, A. Kumar, S. L. Smith, A. W. Chin, J. Clark, T. S. van der Poll, G. C. Bazan and R. H. Friend, *Science*, 2014, **343**, 512–516.
21 B. M. Savoie, A. Rao, A. a. Bakulin, S. Gelinas, B. Movaghar, R. H. Friend, T. J. Marks and M. a. Ratner, *J. Am. Chem. Soc.*, 2014, **136**, 2876–2884.
22 F. Gajdos, H. Oberhofer, M. Dupuis and J. Blumberger, *J. Phys. Chem. Lett.*, 2013, **4**, 1012–1017, DOI: 10.1021/jz400227c.
23 S. Albrecht, K. Vandewal, J. R. Tumbleston, F. S. U. Fischer, J. D. Douglas, J. M. J. Fréchet, S. Ludwigs, H. Ade, A. Salleo and D. Neher, *Adv. Mater.*, 2014, **26**, 2533–2539.
24 J. Idé, D. Fazzi, M. Casalegno, S. V. Meille and G. Raos, *J. Mater. Chem. C*, 2014, 7313–7325.
25 N. R. Tummala, Z. Zheng, S. G. Aziz, V. Coropceanu and J.-L. Brédas, *J. Phys. Chem. Lett.*, 2015, 3657–3662.
26 G. D'Avino, S. Mothy, L. Muccioli, C. Zannoni, L. Wang, J. Cornil, D. Beljonne and F. Castet, *J. Phys. Chem. C*, 2013, **117**, 12981–12990.
27 D. L. Cheung and A. Troisi, *J. Phys. Chem. C*, 2010, **114**, 20479–20488, DOI: 10.1021/jp1049167.
28 H. Oberhofer and J. Blumberger, *Phys. Chem. Chem. Phys.*, 2012, **14**, 13846.
29 H. Li, B. C.-K. Tee, J. J. Cha, Y. Cui, J. W. Chung, S. Y. Lee and Z. Bao, *J. Am. Chem. Soc.*, 2012, **134**, 2760–2765.
30 H. Li, C. Fan, M. Vosgueritchian, B. C.-K. Tee and H. Chen, *J. Mater. Chem. C*, 2014, **2**, 3617.
31 J. C. Aguirre, C. Arntsen, S. Hernandez, R. Huber, A. M. Nardes, M. Halim, D. Kilbride, Y. Rubin, S. H. Tolbert, N. Kopidakis, B. J. Schwartz and D. Neuhauser, *Adv. Funct. Mater.*, 2014, **24**, 784–792.
32 N. R. Tummala, S. Mehraeen, Y. T. Fu, C. Risko and J. L. Brédas, *Adv. Funct. Mater.*, 2013, **23**, 5800–5813.
33 K. M. Pelzer, M. K. Y. Chan, S. K. Gray and S. B. Darling, *J. Phys. Chem. C*, 2014, **118**, 21785–21797.
34 F. Steiner, S. Foster, A. Losquin, J. Labram and T. D. Anthopoulos, *Mater. Horiz.*, 2015, **2**, 113–119.
35 H. Tamura and M. Tsukada, *Phys. Rev. B: Condens. Matter Mater. Phys.*, 2012, **85**, 1–8.
36 P. J. Bounds and R. W. Munn, *Chem. Phys.*, 1979, **44**, 103–112.
37 P. J. Bounds and R. W. Munn, *Chem. Phys.*, 1981, **59**, 41–45.
38 E. A. Silinsh and V. Capek, *Organic Molecular Crystals: Interaction Localization, and Transport Phenomena, American Institute of Physics*, 1997.
39 E. Tsiper and Z. Soos, *Phys. Rev. B: Condens. Matter Mater. Phys.*, 2001, **64**, 1–12.
40 I. I. Fishchuk, V. I. Arkhipov, A. Kadashchuk, P. Heremans and H. Bässler, *Phys. Rev. B: Condens. Matter Mater. Phys.*, 2007, **76**, 1–12.
41 S. Olthof, S. Mehraeen, S. K. Mohapatra, S. Barlow, V. Coropceanu, J. L. Brédas, S. R. Marder and A. Kahn, *Phys. Rev. Lett.*, 2012, **109**, 1–5.
42 H.-B. Bürgi, E. Blanc, D. Schwarzenbach, S. Liu, Y. Lu, M. M. Kappes and J. A. Ibers, *Angew. Chem., Int. Ed. Engl.*, 1992, **31**, 640–643.
43 G. Paternò, A. J. Warren, J. Spencer, G. Evans, V. G. Sakai, J. Blumberger and F. Cacialli, *J. Mater. Chem. C*, 2013, **1**, 5619.
44 M. Casalegno, S. Zanardi, F. Frigerio, R. Po, C. Carbonera, G. Marra, T. Nicolini, G. Raos and S. V. Meille, *Chem. Commun.*, 2013, **49**, 4525–4527.

Published on 25 November 2015. Downloaded by Georgia Institute of Technology on 23/12/2016 16:28:28.

45 L. Muccioli, G. D'Avino and C. Zannoni, *Adv. Mater.*, 2011, **23**, 4532–4536.
46 J. C. Phillips, R. Braun, W. Wang, J. Gumbart, E. Tajkhorshid, E. Villa, C. Chipot, R. D. Skeel, L. Kalé and K. Schulten, *J. Comput. Chem.*, 2005, **26**, 1781–1802.
47 X.-B. Wang, C.-F. Ding and L.-S. Wang, *J. Chem. Phys.*, 1999, **110**, 8217–8220.
48 B. W. Larson, J. B. Whitaker, X.-B. Wang, A. A. Popov, G. Rumbles, N. Kopidakis, S. H. Strauss and O. V. Boltalina, *J. Phys. Chem. C*, 2013, **117**, 14958–14964.
49 R. Nakanishi, A. Nogimura, R. Eguchi and K. Kanai, *Org. Electron.*, 2014, **15**, 2912–2921.
50 X. Qian, P. Umari and N. Marzari, *Phys. Rev. B: Condens. Matter Mater. Phys.*, 2015, **91**, 245105.
51 A. Van Vooren, V. Lemaur, A. Ye, D. Beljonne and J. Cornil, *ChemPhysChem*, 2007, **8**, 1240–1249.
52 J. Huang and M. Kertesz, *J. Chem. Phys.*, 2005, **122**, 234707.
53 A. Kubas, F. Hoffmann, A. Heck, H. Oberhofer, M. Elstner and J. Blumberger, *J. Chem. Phys.*, 2014, **140**, 104105.
54 J. Huang and M. Kertesz, *Chem. Phys. Lett.*, 2004, **390**, 110–115.
55 G. D'Avino, L. Muccioli, C. Zannoni, D. Beljonne and Z. G. Soos, *J. Chem. Theory Comput.*, 2014, **10**, 4959–4971.
56 M. J. Frisch, G. W. Trucks, H. B. Schlegel, G. E. Scuseria, M. A. Robb, J. R. Cheeseman, G. Scalmani, V. Barone, B. Mennucci, G. A. Petersson, H. Nakatsuji, M. Caricato, X. Li, H. P. Hratchian, A. F. Izmaylov, J. Bloino, G. Zheng, J. L. Sonnenberg, M. Hada, M. Ehara, K. Toyota, R. Fukuda, J. Hasegawa, M. Ishida, T. Nakajima, Y. Honda, O. Kitao, H. Nakai, T. Vreven, J. A. Montgomery, Jr., J. E. Peralta, F. Ogliaro, M. Bearpark, J. J. Heyd, E. Brothers, K. N. Kudin, V. N. Staroverov, R. Kobayashi, J. Normand, K. Raghavachari, A. Rendell, J. C. Burant, S. S. Iyengar, J. Tomasi, M. Cossi, N. Rega, J. M. Millam, M. Klene, J. E. Knox, J. B. Cross, V. Bakken, C. Adamo, J. Jaramillo, R. Gomperts, R. E. Stratmann, O. Yazyev, A. J. Austin, R. Cammi, C. Pomelli, J. W. Ochterski, R. L. Martin, K. Morokuma, V. G. Zakrzewski, G. A. Voth, P. Salvador, J. J. Dannenberg, S. Dapprich, A. D. Daniels, Ö. Farkas, J. B. Foresman, J. V. Ortiz, J. Cioslowski and D. J. Fox, *Gaussian 09, Revision A.01*, Gaussian, Inc., Wallingford CT, 2009.
57 L. Muccioli, G. D'Avino, R. Berardi, S. Orlandi, A. Pizzirusso, M. Ricci, O. M. Roscioni and C. Zannoni, *Top. Curr. Chem.*, 2013, **352**, 39–101.
58 Y. Zhong, S. Izawa, K. Hashimoto, K. Tajima, T. Koganezawa and H. Yoshida, *J. Phys. Chem. C*, 2015, **119**, 23–28.
59 M. Williams, N. R. Tummala, S. G. Aziz, C. Risko and J.-L. Brédas, *J. Phys. Chem. Lett.*, 2014, **5**, 3427–3433.
60 V. Coropceanu, J. Cornil, D. A. da Silva Filho, Y. Olivier, R. Silbey and J.-L. Brédas, *Chem. Rev.*, 2007, **107**, 926–952.
61 J. Cornil, S. Verlaak, N. Martinelli, A. Mityashin, Y. Olivier, T. Van Regemorter, G. D'Avino, L. Muccioli, C. Zannoni, F. Castet, D. Beljonne and P. Heremans, *Acc. Chem. Res.*, 2012, **46**, 434–443.
62 F. Castet, G. D'Avino, L. Muccioli, J. Cornil and D. Beljonne, *Phys. Chem. Chem. Phys.*, 2014, **16**, 20279–20290.
63 V. Rühle, C. Junghans, A. Lukyanov, K. Kremer and D. Andrienko, *J. Chem. Theory Comput.*, 2009, **5**, 3211–3223.
64 F. May, B. Baumeier, C. Lennartz and D. Andrienko, *Phys. Rev. Lett.*, 2012, **109**, 1–5.
65 V. D. Mihailetchi, J. K. J. van Duren, P. W. M. Blom, J. C. Hummelen, R. A. J. Janssen, J. M. Kroon, M. T. Rispens, W. J. H. Verhees and M. M. Wienk, *Adv. Funct. Mater.*, 2003, **13**, 43–46.
66 P. Kordt, J. J. M. van der Holst, M. Al Helwi, W. Kowalsky, F. May, A. Badinski, C. Lennartz and D. Andrienko, *Adv. Funct. Mater.*, 2015, **25**, 1955–1971.
67 S. V. Novikov, D. H. Dunlap, V. M. Kenkre, P. E. Parris and a. V. Vannikov, *Phys. Rev. Lett.*, 1998, **81**, 4472–4475.
68 S. V. Novikov and A. V. Vannikov, *J. Phys. Chem.*, 1995, **99**, 14573–14576.
69 K. Akaike, K. Kanai, H. Yoshida, J. Tsutsumi, T. Nishi, N. Sato, Y. Ouchi and K. Seki, *J. Appl. Phys.*, 2008, **104**, 023710.
70 H. Yoshida, *J. Phys. Chem. C*, 2014, **118**, 24377–24382.
71 H. Tamura and I. Burghardt, *J. Am. Chem. Soc.*, 2013, **135**, 16364–16367.

 This journal is © The Royal Society of Chemistry 2016